

Ultrahigh-responsivity waveguide-coupled optical power monitor for Si photonic circuits operating at near-infrared wavelengths

Received: 1 February 2022

Accepted: 22 November 2022

Published online: 09 December 2022

 Check for updates

Takaya Ochiai¹, Tomohiro Akazawa¹, Yuto Miyatake¹, Kei Sumita¹,
Shuhei Ohno¹, Stéphane Monfray², Frederic Boeuf²,
Kasidit Toprasertpong¹, Shinichi Takagi¹ & Mitsuru Takenaka¹✉

A phototransistor is a promising candidate as an optical power monitor in Si photonic circuits since the internal gain of photocurrent enables high responsivity. However, state-of-the-art waveguide-coupled phototransistors suffer from a responsivity of lower than 10^3 A/W, which is insufficient for detecting very low power light. Here, we present a waveguide-coupled phototransistor operating at a $1.3\ \mu\text{m}$ wavelength, which consists of an InGaAs ultrathin channel on a Si waveguide working as a gate electrode to increase the responsivity. The Si waveguide gate underneath the InGaAs ultrathin channel enables the effective control of transistor current without optical absorption by the gate metal. As a result, our phototransistor achieved the highest responsivity of approximately 10^6 A/W among the waveguide-coupled phototransistors, allowing us to detect light of $621\ \text{fW}$ propagating in the Si waveguide. The high responsivity and the reasonable response time of approximately $100\ \mu\text{s}$ make our phototransistor promising as an effective optical power monitor in Si photonic circuits.

The rapid progress in Si photonics over the past decade has made it possible to fabricate large-scale photonic circuits on a Si wafer, which are being widely used as optical interconnection devices in datacenters¹. In addition to optical fiber communication, many applications such as deep learning²⁻⁴, quantum computing⁵⁻⁸, and sensing^{9,10} are emerging for Si programmable photonic circuits¹¹, in which numerous optical phase shifters that can control the optical phase of light propagating in a Si waveguide with an electrical signal are integrated. To reconfigure photonic circuits for a specific purpose, it is crucial to accurately set phase values of all phase shifters. Since an initial phase error of a phase shifter is unavoidable owing to variations in device fabrication, accurate initialization and setting a target phase value are critical issues for programmable photonic circuits.

Various methods have been proposed to configure phase shifters by monitoring outputs of a photonic circuit;^{12,13} however, the simplest and most reliable method is to integrate numerous optical power monitors in a photonic circuit¹⁴⁻¹⁶. For a non-invasive optical power monitoring in a waveguide, monitoring the change in the conductivity of the waveguide caused by optical absorption through capacitive coupling is one of the promising methods¹⁷. However, this method requires a relatively high optical input power and phase-sensitive detection with additional electronics for achieving high sensitivity. Ge photodetectors (PDs) widely used in Si photonic circuits are another candidate for use as an optical power monitor;¹⁸ however, the dark current of a Ge PD is rather high, thereby not suitable for detecting very weak light^{19,20}. Moreover, an additional photonic circuit for

¹Department of Electrical Engineering and Information Systems, The University of Tokyo, 7-3-1 Hongo, Bunkyo-ku, Tokyo 113-8656, Japan. ²STMicroelectronics, 850 Rue Jean Monnet, 38920 Crolles, France. ✉e-mail: takenaka@mosfet.t.u-tokyo.ac.jp

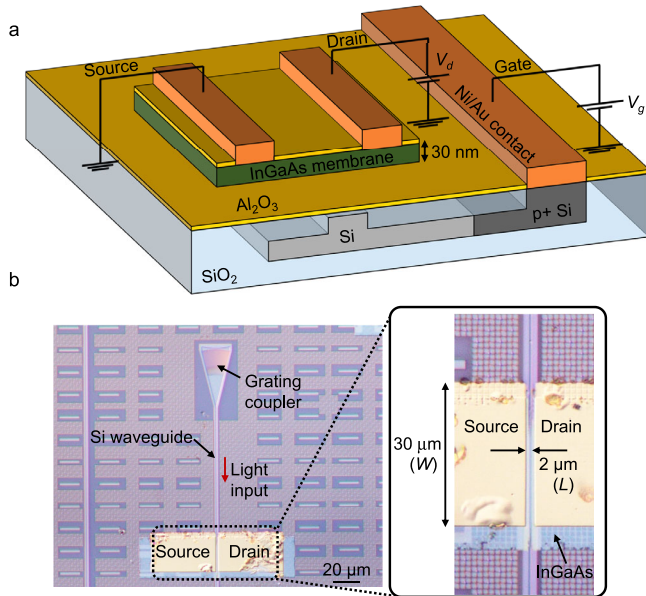


Fig. 1 | Schematic and images of a fabricated waveguide-coupled phototransistor. **a** 3D view of the phototransistor consisting of a 30 nm-thick InGaAs membrane on the Si waveguide back gate with an Al₂O₃ gate dielectric. The Ni/Au metal source and drain are formed on the InGaAs channel. **b** Plan-view microscopy images of the fabricated device. An optical signal at a 1.3 μm wavelength is coupled to the Si waveguide through the grating coupler. The gate length and width are 2 μm and 30 μm, respectively.

tapping optical power and a transimpedance amplifier are required for detection, and as the number of Ge PDs increases, the complexity of photonic and electrical circuits also increases²¹. Therefore, a high-responsivity optical power monitor that can be integrated with Si programmable photonic circuits in a simple manner is essential for reconfiguring their functionality accurately.

Phototransistors based on bipolar junction transistors (BJTs)^{22–26}, junction field-effect transistors (JFETs)^{27,28}, and metal-oxide-semiconductor field-effect transistors (MOSFETs)^{29–42} can have high photosensitivity owing to the amplification of photocurrent. Although BJT-based phototransistors have been developed so far for high-speed optical communication, their responsivity is typically below 10³ A/W because the gain for the photocurrent cannot exceed the gain for the corrector current to the base current. In contrast, MOSFET-based phototransistors called photoFETs can achieve high responsivity. A responsivity exceeding 10⁶ A/W has been reported for surface-illuminated photoFETs. However, a waveguide-coupled photoFET requires a gate electrode near the optical waveguide, which increases optical loss due to optical absorption by the gate metal^{29–31}. To prevent optical absorption by the gate metal, the gate electrode should be placed away from the waveguide, losing effective gating^{42,43}. As a result, high responsivity has not yet been demonstrated for waveguide-coupled photoFETs.

In this work, we present an ultrahigh-responsivity waveguide-coupled phototransistor with an InGaAs ultrathin membrane bonded onto a Si waveguide. We use the Si waveguide as a gate electrode, enabling the effective control of transistor current without optical loss, which can resolve the issue of the current waveguide-coupled photoFETs.

Results

Device structure and fabrication

We propose to use a Si waveguide as a back gate for a waveguide-coupled photoFET. As shown in Fig. 1a, an InGaAs ultrathin membrane is bonded onto a Si waveguide with Al₂O₃ gate dielectric. A gate voltage

can be applied to the InGaAs channel through the p-type Si waveguide, allowing us to eliminate the gate metal that is required for typical waveguide-coupled photoFETs. The effective control of the transistor current flowing in the InGaAs ultrathin channel is achieved while avoiding optical loss due to optical absorption by a gate metal. As a result, we can realize a highly sensitive waveguide-coupled phototransistor. In addition to the superior electrostatic control, with the InGaAs ultrathin membrane, a tapered structure⁴⁴ is no longer required; such a structure requires a complicated fabrication process such as crystal regrowth to suppress the optical reflection at the edge of the Si hybrid waveguide^{45,46}. As a result, the waveguide phototransistor shown in Fig. 1a can be realized with a simple fabrication process (see Methods and Supplementary Section I). In particular, a buried p-type Si gate waveguide can be fabricated by the standard complementary metal-oxide-semiconductor (CMOS) processes such as ion implantation and chemical mechanical polishing. Figure 1b shows a plan-view microscopy image of the fabricated photoFET. A 30 nm-thick p-type InGaAs layer lattice-matched to InP was bonded onto the Si waveguide with 10 nm-thick Al₂O₃ layer. Since the Al₂O₃ layer works as a gate dielectric, the electron inversion layer is formed when a positive gate voltage is applied through the Si waveguide, making the transistor turn on. Since the Schottky contact for holes is formed between the p-type InGaAs and most metals owing to the Fermi level pinning⁴⁷, the metal source and drain were formed by simply depositing Ni/Au electrodes on the InGaAs layer. The low Schottky barrier height for electrons of the Ni/Au metal S/D enables the normal n-channel transistor operation. The channel length *L* of the transistor, defined as the gap between the source and drain metals, was 2 μm. The length of the InGaAs absorber, corresponding to the width of the phototransistor *W*, was designed to be 30 μm. The Ni/Au contact to the Si waveguide back gate was formed on the heavily doped Si slab (see Supplementary Section I). The Si waveguide was designed to obtain a single-mode operation at a 1.3 μm wavelength. A light signal at a 1.3 μm wavelength was injected into the fundamental transverse-electric (TE) mode of the Si waveguide through a grating coupler and absorbed at the 30 nm-thick InGaAs layer.

Transistor characteristics

First, the characteristics as a transistor without light injection were investigated (see Methods and Supplementary Section II). Figure 2a shows the drain current (*I_d*) – gate voltage (*V_g*) characteristics when the drain voltages (*V_d*) were 0.05 V and 0.5 V. By applying a gate voltage to the Si waveguide back gate, we obtained a drain current on/off ratio of ~10⁴, suggesting effective gate control for the transistor channel. Figure 2b shows the *I_d*–*V_d* characteristics when *V_g* was swept from –1 V to 1 V. The saturation of *I_d* with respect to *V_d* was observed, indicating a well-behaved transistor operation. We also prepared the InGaAs transistor for mobility measurement (see Supplementary Section III). The field-effect mobility was estimated to be 608 cm²/V·s from the *I_d*–*V_g* characteristics. The high electron mobility contributes to the high responsivity and the reasonable response time of the proposed InGaAs photoFET as discussed later. Note that the electron mobility in the inversion InGaAs channel is lower than that in lightly doped InGaAs bulk⁴⁸ due to the scattering at the MOS interface. The typical electron mobility in the inversion InGaAs channel is 1000–2000 cm²/V·s⁴⁷. Therefore, there is room for improvement in the electron mobility of our device through process optimization.

Photoresponses

Next, the characteristics of the photoFET were evaluated with light injection (See Methods). Figure 3a shows the *I_d*–*V_d* characteristics at *V_g* of 1 V when the continuous-wave light signal at a 1305 nm wavelength was injected at various input powers. Note that the input power is defined as the intensity coupled to the photoFET by excluding the

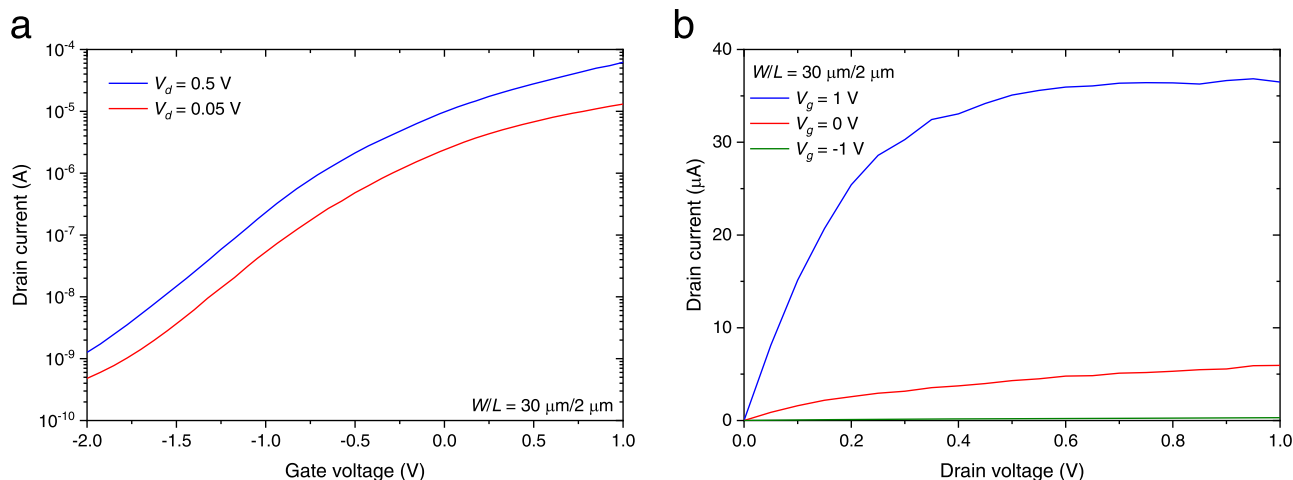


Fig. 2 | Electrical characteristics of a waveguide-coupled InGaAs phototransistor with no light injection. a I_d - V_g characteristics with V_d of 0.05 V and 0.5 V. **b** I_d - V_d characteristics with V_g of -1 V, 0 V, and 1 V.

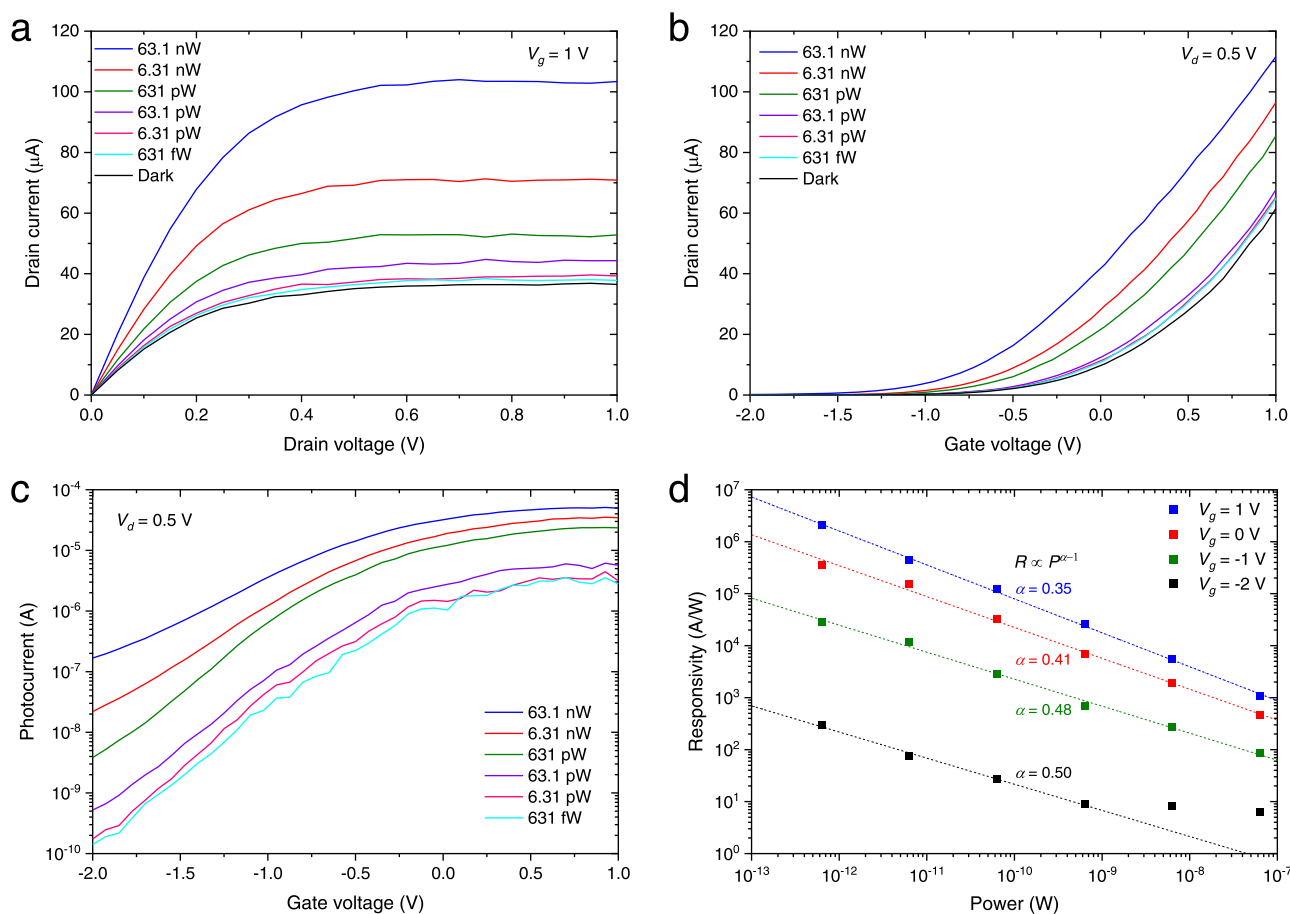


Fig. 3 | Photoresponses of a waveguide-coupled InGaAs phototransistor with light injection of a 1.3 μm wavelength. a I_d - V_d characteristics with V_g of 1 V. **b** I_d - V_g characteristics in the linear scale with V_d of 0.5 V. **c** Photocurrent as a

function of V_g with V_d of 0.5 V. **d** Relationship between responsivity and input power at various gate voltages.

insertion loss of the grating coupler and the Si waveguide (see Supplementary Section IV). The total insertion loss from the grating coupler to the PD is 7.52 dB. The additional insertion loss caused by the photodetector integration can be <0.05 dB owing to the InGaAs ultrathin channel⁴⁴. Because of the photocurrent amplification by the transistor operation, a photocurrent significantly greater than the dark

current was observed even for a very weak light of 631 fW. Figure 3b shows the I_d - V_g characteristics in the linear scale at various input powers when V_d was 0.5 V. It was clearly observed that the threshold voltage of the transistor was shifted by the photogating effect through hole accumulation in the InGaAs channel^{37,39,49}. The photocurrent calculated by subtracting the dark current from the drain current with

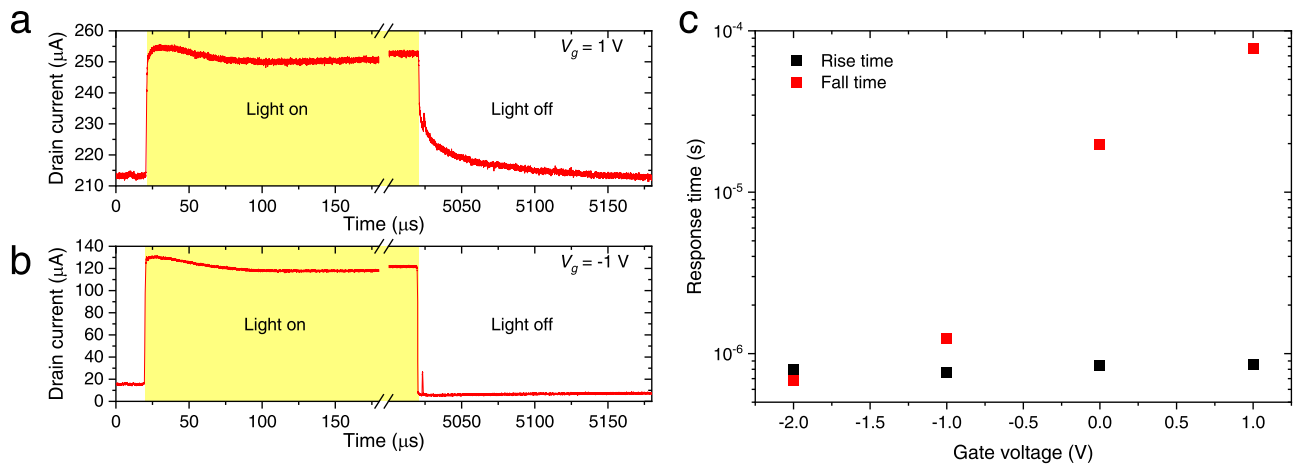


Fig. 4 | Time response of a waveguide-coupled InGaAs phototransistor. a Time response of I_d with V_g of 1 V. **b** Time response of I_d with V_g of -1 V. **c** Rise time and fall time as a function of V_g .

light irradiation is shown in Fig. 3c. A large photocurrent was obtained through the photogating effect when the transistor was in the on state. When the transistor was in the off state, the photoconductive effect might contribute to the amplification of the photocurrent as well as the photogating effect. Figure 3d shows the responsivity R as a function of the input optical power P at various V_g , where R is proportional to $P^{\alpha-1}$. When $\alpha=1$, the photoconductive effect is dominant, whereas when $0 < \alpha < 1$, the photogating effect is dominant^{37,49–51}. It is found that α decreases as V_g increases, suggesting that the photogating effect is more dominant in the on state. The photocurrent component attributable to the photogating effect can be expressed by the product of the transconductance and the threshold voltage shift. Since the transconductance increases as V_g increases, the photocurrent amplified by the photogating effect becomes very large when the phototransistor is in the on state. As a result, when V_g was 1 V, an extremely large responsivity of $\sim 1 \times 10^6$ A/W was obtained at an incident power between 631 fW and 6.31 pW. As discussed later, the absorption of the 30 μm -long phototransistor is estimated to be 6 dB. Hence, the estimated intrinsic responsivity is ~ 0.75 A/W at a 1.3 μm wavelength. As a result, the gain of the photocurrent is ~ 1.3 times greater than the responsivity. Note that the effective refractive index of the guided mode is changed by bonding the InGaAs membrane. However, this change is steady and not an issue for configuring a photonic circuit. When a gate voltage is applied, the carrier accumulation at the MOS interface may affect the effective refractive index and absorption⁵². However, since the device length is 30 μm or potentially much less than 30 μm as described later, the impact of the carrier accumulation is negligible. The leakage current flowing through the gate dielectric is very small when a gate voltage is 1 V. Therefore, there is no impact of the leakage current on our results. The I_d - V_g curve showed small hysteresis due to the electron traps in the InGaAs/ Al_2O_3 interface⁵³. Since the electron traps result in a positive shift in the threshold voltage that is opposite to the photogating effect, the hysteresis does not affect our results.

Time responses

The time response of the photoFET was also evaluated by injecting a modulated optical signal (See Methods). The rise time and fall time of the optical signal generated by direct modulation of a tunable laser were ~ 400 ns and 100 ns, respectively (see Supplementary Section V). Figure 4a shows the time response of I_d when $V_d=0.5$ V and $V_g=1$ V. The rise time of I_d (τ_R) was ~ 1 μs , whereas the fall time (τ_F) was ~ 100 μs , much longer than τ_R . In contrast, when V_g was -1 V, τ_R did not change significantly, whereas τ_F became much shorter (Fig. 4b). The gate voltage dependence of τ_R and τ_F is shown in Fig. 4c. Although τ_R was

almost independent of V_g , τ_F increased exponentially with V_g . When the input light was turned off, the photocurrent induced by the photogating effect decreased owing to the reduction in the number of accumulated holes in the InGaAs channel through carrier recombination. As discussed for Fig. 3d, the photogating effect becomes dominant as V_g increases. As a result, the hole lifetime makes τ_F long. The hole lifetime of ~ 100 μs is two orders of magnitude larger than that in InGaAs bulk⁵⁴ since the electric field in the depletion layer of the InGaAs channel separates electrons and holes, making the hole lifetime long. In contrast, when V_g is negative, there is no depletion layer. Therefore, the hole lifetime becomes close to that in InGaAs bulk⁵⁴, resulting in a short τ_F . Note that the obtained temporal response of ~ 100 μs is sufficiently fast for an optical power monitor in a photonic circuit. For example, the splitting ratio of a Mach-Zehnder interferometer can be calibrated by monitoring the optical powers of two output ports.

Discussion

Figure 5 is the benchmark for phototransistors that shows the relationship between responsivity and response time. Owing to the large optical absorption in the waveguide structure, the proposed waveguide-coupled photoFET exhibits more than three orders of magnitude greater responsivity than the surface-illuminated InGaAs photoFET³². Note that the InGaAs photoFET in Ref. 32 was fabricated on a flexible substrate and its responsivity can potentially be improved using a rigid substrate. PhotoFETs based on 2D materials^{35,37,38,42} show a high responsivity of 10^3 – 10^7 A/W. However, their response time is on the order of 1 s because of the long carrier lifetime of trap states, which is more suitable for image and gas sensor applications. Phototransistors based on BJTs or JFETs exhibit a response time of < 1 ns, while their responsivity is $< 10^2$ A/W, which is suitable for high-speed optical communication applications. In contrast, using the InGaAs ultrathin channel and the Si waveguide gate, our device exhibits the highest responsivity of 10^5 – 10^6 A/W among the waveguide-coupled phototransistors with a sub-millisecond response time, which makes it very suitable for an optical power monitor in Si photonic circuits. The photocurrent induced by the photogating effect (I_{PG}) can be expressed as

$$I_{PG} = g_m \Delta V_{th} = \frac{\Delta Q}{\tau_{tr}} = \frac{g^* \tau_p}{\tau_{tr}}, \quad (1)$$

where g_m is the transconductance, ΔV_{th} is the threshold voltage shift by the photogating effect, ΔQ is the total charge of the photo-generated holes, τ_{tr} is the carrier transit time of an electron⁴⁹, g^* is the

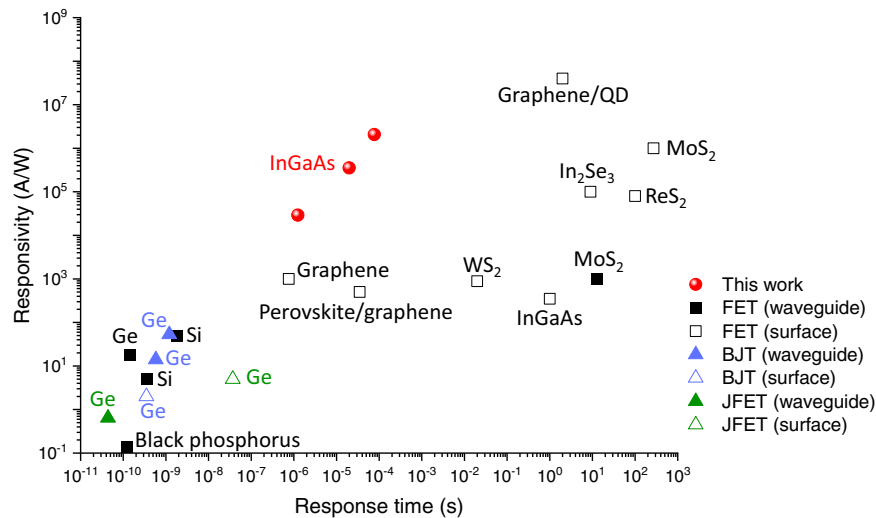


Fig. 5 | Benchmark of responsivity and response time for various phototransistors based on metal-oxide-semiconductor field-effect transistors (MOSFETs), bipolar junction transistors (BJTs), and junction field-effect transistors (JFETs). Comparison of responsivity and response time demonstrated for MOSFET-based phototransistors (waveguide-coupled: Ge³¹, Si⁴³, black

phosphorus²⁹ and MoS₂⁴², surface-illuminated: InGaAs³², graphene/QD³⁴, perovskite/graphene⁴⁰, graphene³⁹, MoS₂³⁵, WS₂⁴¹, In₂Se₃³⁷, and ReS₂³⁸), BJT-based phototransistors (waveguide-coupled: Ge^{22,24}, surface-illuminated: Ge²⁵), and JFET-based phototransistors (waveguide-coupled: Ge²⁷, surface-illuminated: Ge²⁸).

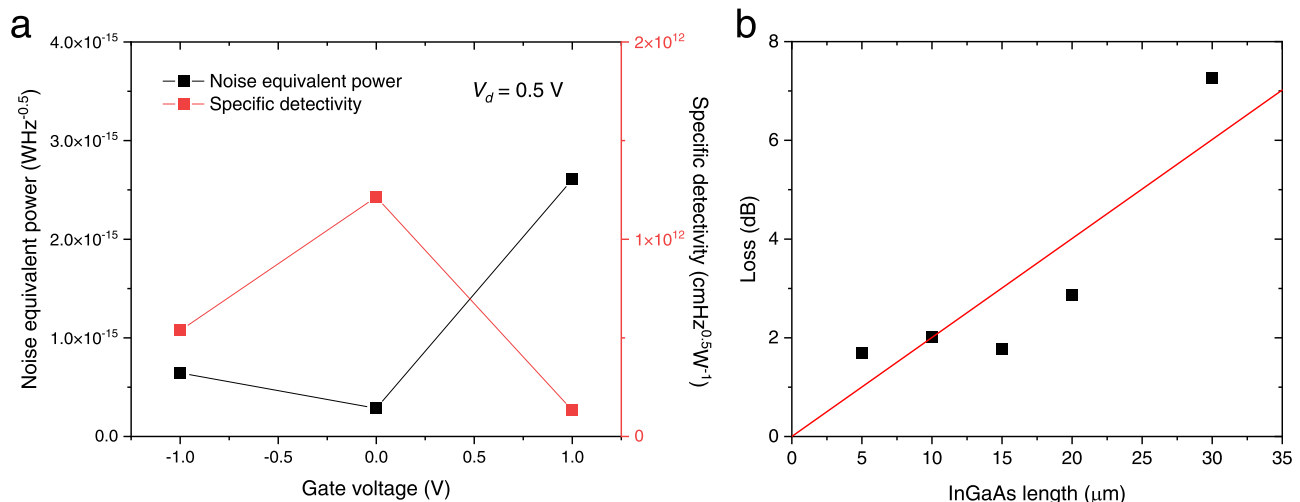


Fig. 6 | Evaluation of noise equivalent power, specific detectivity, and insertion loss. a Measured noise equivalent power and specific detectivity of waveguide-coupled InGaAs phototransistor. The noise equivalent power was extracted from the measured noise power density spectrum with varied gate voltages when V_d was

0.5 V. **b** Insertion loss of the phototransistor as a function of InGaAs length. By measuring the optical transmission of the phototransistor with varied device lengths, the insertion loss was evaluated to be 0.20 dB/μm, suggesting that the insertion loss can be <0.1 dB with 0.5 μm-long device.

generation rate of photoexcitation, and τ_p is the carrier lifetime of holes. The proposed device has a larger ΔQ than the surface-illuminated InGaAs photoFETs because of the large optical absorption in the waveguide configuration. Since the carrier transit time τ_{tr} can be small owing to the high electron mobility in the InGaAs channel, we can increase I_{PG} without increasing τ_p . This is the reason why the proposed InGaAs photoFET can achieve a shorter response time than the phototransistors based on 2D materials with comparable responsivity. Since the electron mobility can be improved by process optimization due to the high electron mobility of InGaAs⁴⁷, there is room for improvement in the responsivity without the expense of the response time.

The noise equivalent power (NEP) and specific detectivity were also evaluated from the measured noise power density spectrum when V_d was 0.5 V (see Supplementary Section VI). As shown in

Fig. 6a, the measured NEP took a minimum value when V_g was 0 V owing to the balance between the dark current and responsivity. As a result, the specific detectivity exceeded 1×10^{12} cm Hz^{1/2} W⁻¹, which is ~100 times greater than that of a Ge photodetector⁵⁵. Hence, our phototransistor exhibits high sensitivity as well as an ultrahigh responsivity.

The insertion loss of the InGaAs photodetector with varied lengths was evaluated as shown in Fig. 6b, taking into account the propagation loss of the Si waveguide and the coupling loss of the grating coupler. As expected, the insertion loss in the log scale was proportional to the InGaAs length. Since the insertion loss per unit length is 0.20 dB/μm, we expect that the insertion loss can be <0.1 dB with the 0.5 μm-long phototransistor. As the device length decreases, the dark current also decreases. In addition, the total number of holes for achieving the same threshold voltage shift also decreases since the

volume of the channel decreases with the device length. Thus, the responsivity of the scaled phototransistor is expected not to degrade markedly. Because of the high responsivity of the phototransistor, we can use it as an optical power monitor even with the device length of much smaller than $0.5\ \mu\text{m}$. Therefore, the proposed waveguide-coupled InGaAs phototransistor can potentially be used as a transparent optical power monitor for a Si waveguide.

In conclusion, we successfully demonstrated the waveguide-coupled photoFET by bonding the InGaAs ultrathin membrane onto the Si waveguide. The InGaAs ultrathin channel enhanced the photogating effect through the Si waveguide gating, resulting in the highest responsivity among the waveguide-coupled phototransistors. The high responsivity and the response time of our phototransistor are sufficient for optical power monitoring and are close to the performance of a commercially available optical power monitor instrument. Owing to the high responsivity, the proposed phototransistor can be a transparent in-line optical power monitor for a Si waveguide realized by reducing the length of the InGaAs absorber to $<1\ \mu\text{m}$. If 10 dB insertion loss is acceptable, up to 100 photoFETs can be cascaded, enabling a 100×100 Si programmable photonic circuit. When the photoFET is biased with $V_g = 1\ \text{V}$ and $V_d = 0.5\ \text{V}$, the transistor current is $\sim 40\ \mu\text{A}$, meaning that the power consumption of the single photoFET is $\sim 20\ \mu\text{W}$. In the case of a 100×100 Si programmable photonic circuit where $\sim 10,000$ monitor photoFETs should be required, the total power consumption of the photoFETs is $\sim 200\ \text{mW}$. This power consumption can be reduced further by reducing the device length. Therefore, the power consumption does not limit the device density. Hence, the waveguide-coupled InGaAs photoFET with a Si waveguide gate can be used as an effective optical power monitor in Si programmable photonic circuits for communication, computing, and sensing applications.

Methods

The InGaAs photoFET was fabricated as follows (see Supplementary Section I for the detailed fabrication procedure). A 30 nm-thick p-type $\text{In}_{0.53}\text{Ga}_{0.47}\text{As}$ membrane was bonded onto the Si waveguide with 10 nm-thick Al_2O_3 bonding interface. After the patterning of the InGaAs membrane, Ni/Au contact pads were formed as the source, drain, and gate by lift-off. The electrical characteristics of the photoFET were measured using a semiconductor parameter analyzer (Agilent Technologies, 4156 C). The photoresponse of the photoFET was measured at a wavelength of 1305 nm. A tunable laser (Santec, TSL-510) was used as a fiber-coupled light source. The input power was tuned using a variable optical attenuator (Anritsu, MN9605C). The polarization of the input light was adjusted to the TE mode of the Si waveguide by an in-line polarization controller. The input light was coupled from a single-mode fiber to the Si waveguide through the grating coupler. For the time response measurement, the tunable laser was modulated using an electrical waveform generator (Agilent, 33522B). The electrical waveform was recorded using a waveform generator/fast measurement unit (Agilent, B1530A) of a semiconductor device analyzer (Agilent Technologies, B1500A).

Data availability

The data that support the findings of this study are available from the corresponding authors on reasonable request.

Code availability

The code that used for the simulation is available at <https://doi.org/10.5281/zenodo.7281340>.

References

- Siew, S. Y. et al. Review of silicon photonics technology and platform development. *J. Lightwave Technol.* **39**, 4374–4389 (2021).
- Shen, Y. et al. Deep learning with coherent nanophotonic circuits. *Nat. Photon.* **11**, 441–446 (2017).
- Ohno, S., Toprasertpong, K., Takagi, S. & Takenaka, M. Si microring resonator crossbar arrays for deep learning accelerator. *Jpn. J. Appl. Phys.* **59**, 2–8 (2020).
- Shastri, B. J. et al. Photonics for artificial intelligence and neuro-morphic computing. *Nat. Photon.* **15**, 102–114 (2021).
- Carolan, J. et al. Universal linear optics. *Science* **349**, 711–716 (2015).
- Harris, N. C. et al. Quantum transport simulations in a programmable nanophotonic processor. *Nat. Photon.* **11**, 447–452 (2017).
- Paesani, S. et al. Generation and sampling of quantum states of light in a silicon chip. *Nat. Phys.* **15**, 925–929 (2019).
- Arrazola, J. M. et al. Quantum circuits with many photons on a programmable nanophotonic chip. *Nature* **591**, 54–60 (2021).
- Sun, J., Timurdogan, E., Yaacobi, A., Hosseini, E. S. & Watts, M. R. Large-scale nanophotonic phased array. *Nature* **493**, 195–199 (2013).
- Ito, H. et al. Wide beam steering by slow-light waveguide gratings and a prism lens. *Optica* **7**, 47–52 (2020).
- Bogaerts, W. et al. Programmable photonic circuits. *Nature* **586**, 207–216 (2020).
- Pérez-López, D., López, A., DasMahapatra, P. & Capmany, J. Multi-purpose self-configuration of programmable photonic circuits. *Nat. Commun.* **11**, 6359 (2020).
- Hamerly, R., Bandyopadhyay, S. & Englund, D. Robust zero-change self-configuration of the rectangular mesh. In *Optical Fiber Communication Conference*, Tu5H.2 (OSA, 2021).
- Miller, D. A. Self-aligning universal beam coupler. *Opt. Express* **21**, 6360–6370 (2013).
- Miller, D. A. Self-configuring universal linear optical component [Invited]. *Photon. Res.* **1**, 1 (2013).
- Miller, D. A. Setting up meshes of interferometers – reversed local light interference method. *Opt. Express* **25**, 29233 (2017).
- Morichetti, F. et al. Non-invasive on-chip light observation by contactless waveguide conductivity monitoring. *IEEE J. Sel. Top. Quant. Electron.* **20**, 292–301 (2014).
- Michel, J., Liu, J. & Kimerling, L. C. High-performance Ge-on-Si photodetectors. *Nat. Photon.* **4**, 527–534 (2010).
- Takenaka, M., Morii, K., Sugiyama, M., Nakano, Y. & Takagi, S. Dark current reduction of Ge photodetector by GeO_2 surface passivation and gas-phase doping. *Opt. Express* **20**, 8718–8725 (2012).
- Chen, H. et al. Dark current analysis in high-speed germanium p-i-n waveguide photodetectors. *J. Appl. Phys.* **119**, 213105 (2016).
- Pantouvaki M. et al. 20Gb/s silicon ring modulator co-integrated with a Ge monitor photodetector. In 39th European Conference and Exhibition on Optical Communication, We.3.B.2 (IET, 2013).
- Going, R., Seok, T. J., Loo, J., Hsu, K. & Wu, M. C. Germanium wrap-around photodetectors on silicon photonics. *Opt. Express* **23**, 11975–11984 (2015).
- Sorianello, V. et al. High responsivity SiGe heterojunction phototransistor on silicon photonics platform. *Opt. Express* **23**, 28163–28169 (2015).
- Frounchi, M., Tzintzarov, G. N., Ildefonso, A. & Cressler, J. D. High responsivity Ge phototransistor in commercial CMOS Si-photonics platform for monolithic optoelectronic receivers. *IEEE Electron Device Lett.* **42**, 196–199 (2021).
- Ang, K. W., Yu, M. B., Lo, G. Q. & Kwong, D. L. Low-voltage and high-responsivity germanium bipolar phototransistor for optical detections in the near-infrared regime. *IEEE Electron Device Lett.* **29**, 1124–1127 (2008).
- Wang, L. S. et al. A new edge-coupled two-terminal double heterojunction phototransistor (ECTT-DHPT) and its DC characteristics. In PhotonicsGlobal@Singapore, 1–3 (IEEE, 2008).

27. Wang, J., Yu, M., Lo, G., Kwong, D. L. & Lee, S. Silicon waveguide integrated germanium JFET photodetector with improved speed performance. *IEEE Photon. Technol. Lett.* **23**, 765–767 (2011).
28. Sahni, S., Luo, X., Liu, J., Xie, Y. H. & Yablonoitch, E. Junction field-effect-transistor-based germanium photodetector on silicon-on-insulator. *Opt. Lett.* **33**, 1138–1140 (2008).
29. Youngblood, N., Chen, C., Koester, S. J. & Li, M. Waveguide-integrated black phosphorus photodetector with high responsivity and low dark current. *Nat. Photon.* **9**, 247–252 (2015).
30. Huang, L. et al. Integration of 2D black phosphorus phototransistor and silicon photonics waveguide system towards mid-infrared on-chip sensing applications. In *Symposium on VLSI Technology*, 161–162 (IEEE, 2018).
31. Going, R. W., Loo, J., Liu, T. J. K. & Wu, M. C. Germanium gate photoMOSFET integrated to silicon photonics. *IEEE J. Sel. Top. Quant. Electron.* **20**, 1–7 (2014).
32. Li, Y. et al. A flexible InGaAs nanomembrane PhotoFET with tunable responsivities in near- and short-wave IR region for lightweight imaging applications. *APL Mater.* **7**, 031503 (2019).
33. Maeda, T. et al. InGaAs photo field-effect-transistors (photoFETs) on half-inch Si wafer using layer transfer technology. *Jpn. J. Appl. Phys.* **59**, SGGE03 (2020).
34. Konstantatos, G. et al. Hybrid graphene–quantum dot phototransistors with ultrahigh gain. *Nat. Nanotechnol.* **7**, 363–368 (2012).
35. Nur, R. et al. High responsivity in MoS₂ phototransistors based on charge trapping HfO₂ dielectrics. *Commun. Mater.* **1**, 1–9 (2020).
36. Choi, W. et al. High-detectivity multilayer MoS₂ phototransistors with spectral response from ultraviolet to infrared. *Adv. Mater.* **24**, 5832–5836 (2012).
37. Island, J. O., Blanter, S. I., Buscema, M., van der Zant, H. S. & Castellanos-Gomez, A. Gate controlled photocurrent generation mechanisms in high-gain In₂Se₃ phototransistors. *Nano Lett.* **15**, 7853–7858 (2015).
38. Liu, E. et al. High responsivity phototransistors based on few-layer ReS₂ for weak signal detection. *Adv. Funct. Mater.* **26**, 1938–1944 (2016).
39. Guo, X. et al. High-performance graphene photodetector using interfacial gating. *Optica* **3**, 1066–1070 (2016).
40. Lee, Y. et al. High-performance perovskite–graphene hybrid photodetector. *Adv. Mater.* **27**, 41–46 (2015).
41. Huo, N. et al. Photoresponsive and gas sensing field-effect transistors based on multilayer WS₂ nanoflakes. *Sci. Rep.* **4**, 5209 (2015).
42. Marin, J. F. G. et al. MoS₂ photodetectors integrated with photonic circuits. *npj 2D Mater. Appl.* **3**, 1–6 (2019).
43. Geis, M. W. et al. Silicon waveguide infrared photodiodes with >35 GHz bandwidth and phototransistors with 50 AW⁻¹ response. *Opt. Express* **7**, 5193–5204 (2009).
44. Ohno, S. et al. Taperless Si hybrid optical phase shifter based on a metal-oxide-semiconductor capacitor using an ultrathin InP membrane. *Opt. Express* **28**, 35663–35673 (2020).
45. Kurczveil, G., Pintus, P., Heck, M. J., Peters, J. D. & Bowers, J. E. Characterization of insertion loss and back reflection in passive hybrid silicon tapers. *IEEE Photon. J.* **5**, 6600410 (2013).
46. Aihara, T. et al. Membrane buried-heterostructure DFB laser with an optically coupled III-V/Si waveguide. *Opt. Express* **27**, 36438–36448 (2019).
47. Kim, S. H. et al. High Performance extremely thin body InGaAs-on-insulator metal-oxide-semiconductor field-effect transistors on Si substrates with Ni-InGaAs metal source/drain. *Appl. Phys. Express* **4**, 114201 (2011).
48. Sotoodeh, M., Khalid, A. H. & Rezazadeh, A. A. Empirical low-field mobility model for III–V compounds applicable in device simulation codes. *J. Appl. Phys.* **87**, 2890–2900 (2000).
49. Fang, H. & Hu, W. Photogating in low dimensional photodetectors. *Adv. Sci.* **4**, 1700323 (2017).
50. Li, L. et al. T. Few-layered PtS₂ phototransistor on h-BN with high gain. *Adv. Funct. Mater.* **27**, 1701011 (2017).
51. Huang, H. et al. Highly sensitive visible to infrared MoTe₂ photodetectors enhanced by the photogating effect. *Nanotechnology* **27**, 445201 (2016).
52. Han, J.-H. et al. Efficient low-loss InGaAsP/Si hybrid MOS optical modulator. *Nat. Photon.* **11**, 486–490 (2017).
53. Lin, J. et al. An investigation of capacitance-voltage hysteresis in metal/high-k/In_{0.53}Ga_{0.47}As metal-oxide-semiconductor capacitors. *J. Appl. Phys.* **114**, 144105 (2013).
54. Walker, A. W. & Denhoff, M. W. Heavy and light hole minority carrier transport properties in low-doped n-InGaAs lattice matched to InP. *Appl. Phys. Lett.* **111**, 162107 (2017).
55. Lin, Y., Lee, K. H., Son, B. & Tan, C. S. Low-power and high-detectivity Ge photodiodes by in-situ heavy As doping during Ge-on-Si seed layer growth. *Opt. Express* **29**, 2940–2952 (2021).

Acknowledgements

This work was partly based on results obtained from projects (JPNP14004, JPNP16007 received by M.T.) commissioned by the New Energy and Industrial Technology Development Organization (NEDO) and partly supported by JST, CREST (JPMJCR2004 received by M.T.). Part of this work was conducted at Takeda Sentanchi super cleanroom, The University of Tokyo, supported by “Nanotechnology Platform Program” of the Ministry of Education, Culture, Sports, Science and Technology (MEXT), Japan, Grant Number JPMXP09F20UT0021. The authors thank Dr. H. Yagi, Dr. Y. Itoh, and Dr. H. Mori of Sumitomo Electric for providing InP epitaxial wafers.

Author contributions

T.O. contributed to fabrication, measurement, and paper preparation. T.A. contributed to measurement. Y.M. contributed to simulation. K.S. and S.O. contributed to the fabrication and analysis. S.M. and F.B. contributed to design and fabrication of the Si waveguide. K.T. and S.T. contributed to the overall discussion. M.T. contributed to the idea, discussion, and paper revision and also provided high-level project supervision.

Competing interests

The authors declare no competing interests.

Additional information

Supplementary information The online version contains supplementary material available at <https://doi.org/10.1038/s41467-022-35206-4>.

Correspondence and requests for materials should be addressed to Mitsuru Takenaka.

Peer review information *Nature Communications* thanks the other anonymous reviewer(s) for their contribution to the peer review of this work. Peer review reports are available.

Reprints and permissions information is available at <http://www.nature.com/reprints>

Publisher’s note Springer Nature remains neutral with regard to jurisdictional claims in published maps and institutional affiliations.

Open Access This article is licensed under a Creative Commons Attribution 4.0 International License, which permits use, sharing, adaptation, distribution and reproduction in any medium or format, as long as you give appropriate credit to the original author(s) and the source, provide a link to the Creative Commons license, and indicate if changes were made. The images or other third party material in this article are included in the article's Creative Commons license, unless indicated otherwise in a credit line to the material. If material is not included in the article's Creative Commons license and your intended use is not permitted by statutory regulation or exceeds the permitted use, you will need to obtain permission directly from the copyright holder. To view a copy of this license, visit <http://creativecommons.org/licenses/by/4.0/>.

© The Author(s) 2022